Recovering Deterministic Behavior from Experimental Time Series in Mixing Reactor

C. Letellier, L. Le Sceller and G. Gouesbet
LESP/UMR CNRS 6614-CORIA, 76131 Mont Saint-Aignan Cedex, France

F. Lusseyran, A. Kemoun and B. Izrar
LEMTA/URA CNRS 875, 54504 Vandoeuvre-les-Nancy Cedex, France

The velocity field in a standard mixing reactor with a Rushton impeller is analyzed by using techniques from the theory of nonlinear dynamical systems. It is shown that the dynamical behavior contains a quasi-periodic motion with three frequencies, f_p, the frequency associated with the rotation of blades, $f_p/6$, and a third frequency f'. Relying on an evaluation of the correlation dimension equal to 3.9, the phase space is likely to be at least four-dimensional. Moreover, a set of four ordinary differential equations is indeed automatically obtained by using a global vector field reconstruction technique, confirming the existence of a 4-D-deterministic behavior contributing to the dynamics of the system.

Introduction

The study and understanding of mixing processes is an important task, relevant to the determination of the working parameters which optimize the mixing efficiency. As a contribution to this goal, the velocity field generated in a standard reactor with a Rushton turbine impeller is investigated by using a nonintrusive measuring technique, namely laser doppler anemometry (Kemoun, 1995). As is well known, mixing processes may be described by nonlinear dynamics and eddy interactions arising from the nonlinearity of the Navier-Stokes equations. The dynamical analysis may therefore be achieved by using tools from the theory of nonlinear dynamical systems if we take care of a separation between deterministic large eddy structures (like the ones simulated in large eddy simulation, LES) and small eddy structures associated with stochasticity in turbulence modeling. In the language of the theory of nonlinear dynamics, determinism is actually associated with a small number of degrees of freedom and stochasticity with a large number of degrees of freedom. In this article, our objective is therefore to extract the deterministic part of the dynamics related to the rotation of blades from the stochastic part associated with small turbulent structures, and to characterize it. The extraction of the large eddy contribution is achieved by applying a Hilbert transform to the experimental time series of the tangential velocity. This deterministic part is thereafter analyzed by working in a phase space reconstructed following a technique put forward by Packard et al. (1980). The phase portrait is first investigated by using classical techniques discovered by Poincaré (1952) such as Poincaré sections and first-return maps. Besides, we also use more recent tools such as symbolic dynamics (Collet and Eckman, 1980; Bai Lin, 1989; Hall, 1994) or global vector field reconstructions (Brown et al., 1994; Gouesbet and Letellier, 1994; Tufillaro et al., 1995; Letellier et al., 1995) to characterize the dynamics of the velocity field. In particular, the success of a global vector field reconstruction may be seen as a confirmation of the existence of a deterministic behavior.

A description is provided of the experimental setup describing the way in which the Hilbert transform is used to separate the deterministic contribution associated to large eddies from the stochastic contribution associated to the small structures of turbulence. An analysis of the phase portrait generated by the deterministic contribution is presented. The automatic reconstruction of a set of ordinary differential equations confirming the deterministic character of the large eddy structure is described followed by a conclusion.

Experimental Time Series

Experimental setup

The reactor is a standard cylindrical vessel in which a Rushton turbine is used for stirring a transparent oil. The tank has a diameter D equal to 0.2 m and contains four baf-

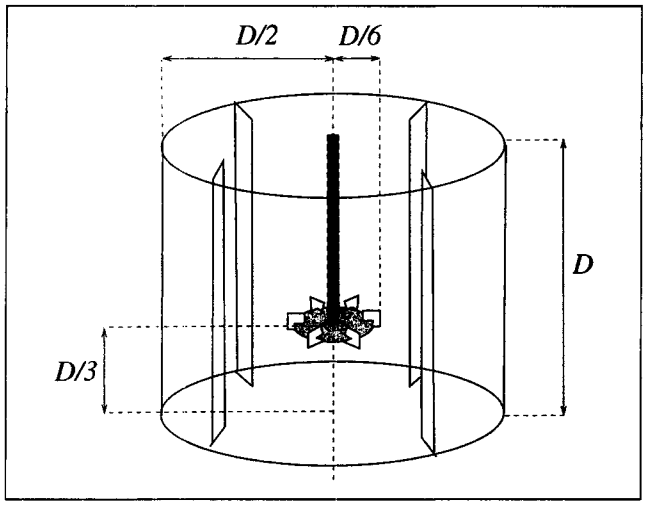

Figure 1. Standard tank with a Rushton rotator.

fles, as in Figure 1. The reactor is a made out from a transparent material (plexiglass) and the oil is refractive index matched to the reactor material, allowing an easy optical access at any point and any time in the flow field.

For the so-called standard tank, the geometry of the rotator is completely determined by a single characteristic length, here taken as being the diameter D of the tank. The height of the tank is equal to D too. The rotator has an outer diameter equal to $D/3$ and is located at a distance $D/3$ from the bottom of the tank. The agitator is a Rushton turbine consisting of a disk with six rectangular blades of width $D/15$ and length $D/12$. In the present experiments, the rotation speed is maintained at 88 rpm, corresponding to a characteristic frequency f_i equal to 1.46 ± 0.06 Hz.

Deterministic component of time series

By using a laser doppler anemometer, two components of the velocity field are simultaneously recorded, namely the radial component v_R and the tangential component v_T. The control volume is located at 5 mm from the blades in the pumping flow which is displayed in Figure 2. The system used is a Doppler frequency tracker DISA 55 N with analog output manufactured by Dantec. The frequency range of the output is 0-6.3 kHz, for the frequency shift of the Bragg cell used for these measurements. The signal is sampled at a frequency f_s equal to 1,024 Hz and 2^{16} points constitute a complete time-series record. A part of each time series is displayed in Figure 3.

From Figure 3, it is apparent that the velocity time series, measured in the vicinity of the turbine blades, cannot be generated by turbulent fluctuations around a constant mean value. It seems obvious that we are facing a combination of a dominant nearly periodic component and of a stochastic residue. This is confirmed by the structure of the power spectrum (Figure 4). The Fourier domain exhibits a frequency packed behavior. This bandwise organization is typical of f-modulated signals. This last property is used to extract a quasi-periodic component from the measured signal. Two steps are needed.

In the first step, the frequency modulation is obtained by spanning the signal into an amplitude and a phase function

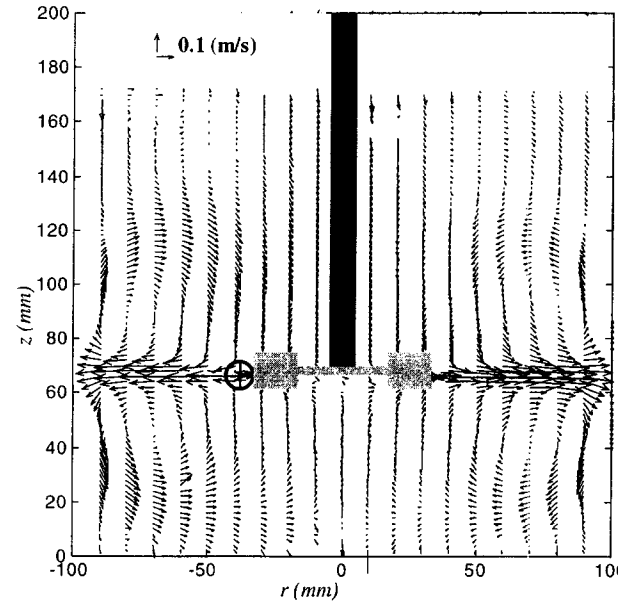

Figure 2. Radial and axial mean field components.
The cross denotes the control volume location.

$\varphi(t)$, using the Hilbert transform. This transform is applied to the time band-pass filtered time series of the tangential component v_T of the velocity. As we are only interested in the modulation of the carrier frequency f_p, the bandwidth $[0, 2\ f_p]$ of the filtered time series is used in order to obtain $\varphi(t)$ (Melville, 1983). We then indeed observe a slow nonperiodic modulation of the instantaneous frequency (Figure 5) around f_p.

Let us now recall the definition and main properties of the Hilbert transform. The Hilbert transform $\tilde{s}(t)$ of a signal $s(t)$ is defined so that the complex function

$$z(t) = s(t) + i\tilde{s}(t) = a(t)e^{i\varphi(t)} \tag{1}$$

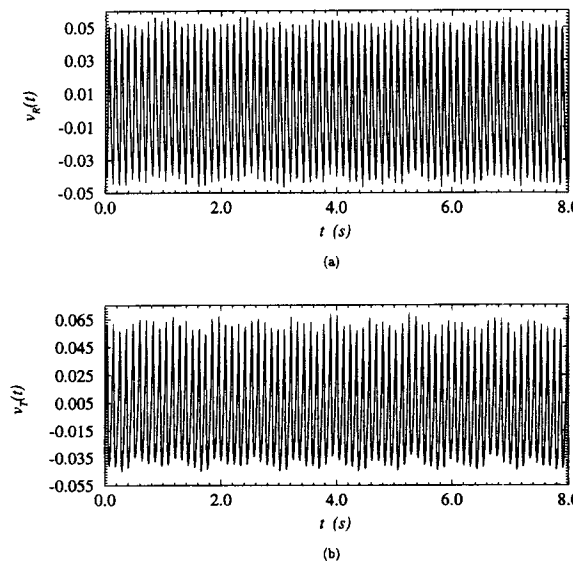

Figure 3. Time series of the two measured components of the velocity field.
(a) Radial component v_R; (b) tangential component v_T.

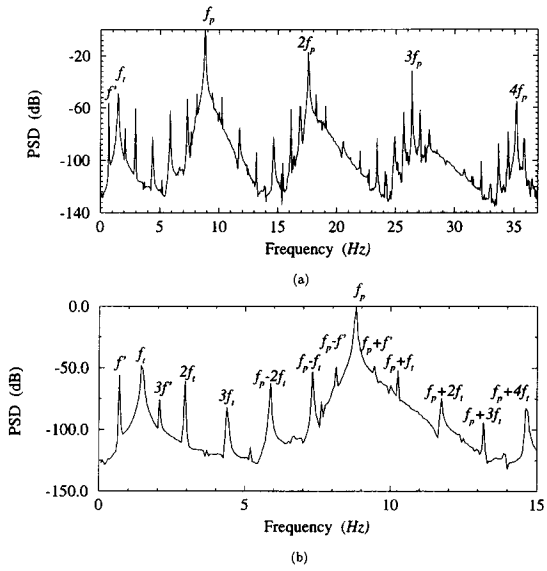

Figure 4. Power spectrum averaged over four spectra computed with 2^{14} points from (a) the tangential component $v_T(t)$; (b) a zoom of this spectrum for the frequency range [0, 15 Hz].

is an analytic function of time, given that $\tilde{s}(t)$ is the convolution product between the original time series and $1/\pi t$. The amplitude $a(t)$ of the function $z(t)$ then describes the envelope of the signal. The phase derivative gives the instantaneous pulsation $\omega(t) = d\varphi(t)/dt$ (Oppenheim and Schafer, 1975).

In the second step, we consider, in a detailed way, the spectrum of the velocity time series, computed by averaging over four spectra, each of them being made out of 2^{14} points, with the sampling frequency f_s (Figure 4). The averaged spectrum exhibits a background noise and a great number of peaks resulting from linear combinations of three principal frequencies, namely the blade passage frequency f_p, the turbine frequency $f_t = f_p/6$, and an unexpected frequency f' related to f_t by $f_t/f' \approx 2.2$. The deterministic part v_D of the velocity component v_T is then obtained by summing the main frequencies given by linear combinations of these three principal frequencies. The summation is made out of 44 terms containing frequencies f_k up to $4f_p$ with a cutoff frequency of 35 Hz, that is, we have

$$v_D = \sum_{k=1}^{44} \left[a_k \cos\left(\frac{f_k}{f_p}\varphi(t)\right) + b_k \sin\left(\frac{f_k}{f_p}\varphi(t)\right)\right] \quad (2)$$

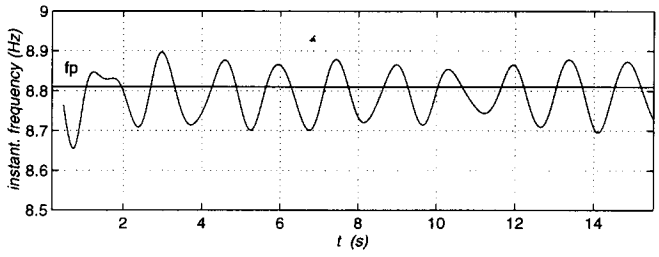

Figure 5. Instantaneous modulation of the main frequency f_p.

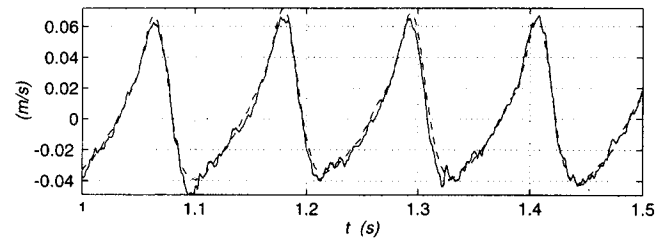

Figure 6. Original signal v_T (plain) and its deterministic part v_D (dashed).

The coefficients a_k and b_k are evaluated by minimizing the squared norm $\| v_T - v_D \|^2$ of the difference $v_t - v_D$. The identified deterministic component v_D looks like a low-pass filtered signal, but preserves some amount of small-scale fluctuations (Figure 6). Also, the nonlinear dependence on time of $\varphi(t)$ is such that v_D exhibits a nonperiodic behavior. The origin of the frequency f', which plays an important role in the structure of the dynamics, is not completely understood. Nevertheless, we might invoke a hydrodynamical origin, such as due to the existence of a tornado spinning around the tank axis. Another possibility could be that the frequency f' characterizes the mechanical driving system. The fact that the ratio f_t/f' remains close to 2.2. when the rotation speed is varied leads us to favor this second possibility.

The analysis of the deterministic contribution is now to be studied, focusing our attention to the tangential component v_T. For the radial component, we shall be content with checking that it contains the same dynamical information as the tangential component.

Dynamical Analysis

Fourier spectrum

In order to determine the relevant characteristic time scales of the dynamics, a Fourier spectrum of the deterministic part is computed in the same way as above (Figure 4). This averaged spectrum has the same characteristics as the one of the whole signal. In particular, the three fundamental frequencies are again exhibited, namely f_p, f_t and f' generating many peaks at values corresponding to their linear combinations (see Table 1).

As the spectrum presents peaks at $(f_p - f')$ and $(f_p + f')$, the dynamics involves a nonlinear coupling between two oscillators, one associated with the blade frequency of the Rushton agitator and one corresponding to the frequency f'. Indeed, we have

$$\sin(2\pi f_p t)\sin(2\pi f' t) = \frac{1}{2}\left[\cos(2\pi\,|\,f_p - f'\,|\,t) - \cos(2\pi\,|\,f_p + f'\,|\,t)\right] \quad (3)$$

Table 1. Linear Combinations of Frequencies f_p, f_t and f'

Frequency (Hz)	0.67	1.46	2.03	2.93	4.39
Combination	f'	f_t	$3f'$	$2f_t$	$3f_t$
Frequency (Hz)	7.33	8.12	8.80	9.47	10.25
Combination	$f_p - f_t$	$f_p - f'$	f_p	$f_p + f'$	$f_p + f_t$

Table 2. Coefficient Spectrum $\{k_p\}$ of the Approximated Function $\tilde{F}$

p	K_p	p	K_p
1	$-5.0007388427366\times10^{-6}$	34	−11,142,240.650981
2	$1.7153701357326\times10^{-4}$	35	6,149,111.8457434
3	$-4.0139649700713\times10^{-3}$	36	1.5087157825452
4	$-4.1878375322953\times10^{-2}$	37	−26.241801686643
5	$-5.5146223710237\times10^{-2}$	38	219.25940771633
6	$-6.6038270128164\times10^{-3}$	39	460.37115519127
7	$-5.1283012300929\times10^{-2}$	40	1,844.0434610508
8	−1.5844290910813	41	−15,664.550341124
9	−5.6506069683103	42	183,526.73839904
10	0.18815674708878	43	−59,147.985547812
11	5.6694836609105	44	−440,524.62217601
12	−15.887246701382	45	2,601,991.1381555
13	16.846827272719	46	12,354.595600511
14	−375.59788997074	47	125,029.63394663
15	2,072.1435902805	48	518,083.98956141
16	$-3.6261653160868\times10^{-2}$	49	−1,135,021.0803142
17	−0.44943217464793	50	8,950,948.1958440
18	9.1805462167562	51	−23,572,896.246735
19	76.384989131116	52	−4,486,557.9677345
20	−79.304588808845	53	−29,470,120.340638
21	−180.37347797477	54	124,423,494.10973
22	−5,641.4931859487	55	−592,909,205.48492
23	−1,942.0428370436	56	−146,012.03560659
24	9,400.7641731195	57	−84,074.308280830
25	−20,3929.48985406	58	−12,628,797.210408
26	918.91555971307	59	935,201.45902407
27	−2,148.8933065770	60	6,180.0040393807
28	64,301.873696486	61	−589,210,231.03263
29	−43,061.850369787	62	−20,800,453.712244
30	−206,873.55926468	63	14,229,075.404375
31	1,559,614.2013169	64	−731,536,848.78563
32	−197,791.64166003	65	−9,357,212,603.7333
33	−957,305.85336854		

A similar remark is valid for the frequencies $(f_p + f_t)$ and $(f_p - f_t)$. Consequently, the dynamics of the tangential velocity component corresponds to a quasi-periodic motion induced by a nonlinear coupling between three frequencies. Also, relying on the computation of a correlation dimension which is found to be equal to 3.9 (Kemoun, 1995; Grassberger and Procaccia, 1983), we expect that the dimension of the embedding space is at least equal to 4.

Phase portrait

The velocity field is governed by a nonlinear dynamics whose evolution may be described in a reconstructed phase space. Starting from a scalar time series, a reconstructed phase space may be generated, equivalently spanned by delay or derivative coordinates (Packard et al., 1980). When using delay coordinates, the evolution of the dynamics of the tangential velocity v_T is displayed in the reconstructed phase space by tracking the time-valued vector

$$\{v_T(t), v_T(t+\tau), \ldots, v_T[t+(d_E-1)\tau]\}$$

where τ is a time delay and d_E is the embedding dimension, that is, the dimension of the reconstructed phase space. The values of the reconstruction parameters (τ and d_E) are of crucial importance for the quality of the phase portrait.

The time delay τ must typically be taken in the range $[0, T_0/2]$, where T_0 is the pseudo-period of the dynamics (Buzug and Pfister, 1992). In the case of our experiments, the pseudo-period is given by f_p^{-1}, that is, it is associated with the fundamental frequency of largest amplitude in the Fourier spectrum. Then, in a simple case as the one here considered, the time delay τ may easily be chosen by visual inspection of phase portraits. In more complicated cases, an algorithm based on the first minimum of the mutual information (Fraser and Swinney, 1986) may automatically provide an optimal time delay (Abarbanel et al., 1993).

The embedding dimension d_E may be obtained according to Taken's theorem (Takens 1980) derived from Whitney's theorem, namely, we are ensured of a good reconstruction (by good reconstruction, we mean that there exists a diffeomorphism Φ between the original phase space, in general unknown, and the reconstructed phase space spanned by the reconstructing coordinates) if d_E is greater than or equal to $2D_2+1$ where D_2 is the correlation dimension. This may be computed by using the Grassberger-Procaccia algorithm (Grassberger and Procaccia, 1983). Here, D_2 is taken as an approximation of the Haussdorff-Besicovitch dimension. Nevertheless, Takens' criterion is a sufficient one and not a necessary one. As a matter of fact, it has been shown that a space whose dimension is smaller than $2D_2+1$ may possibly be safely used (Letellier and Gouesbet, 1996) and, in particular, when d_E is equal to $[\text{int}(D_2)+1]$.

In the present case, we expect that we are facing a dynamics which may be embedded in a $4D$ space. Consequently, we use a space reconstructed with four variables as follows

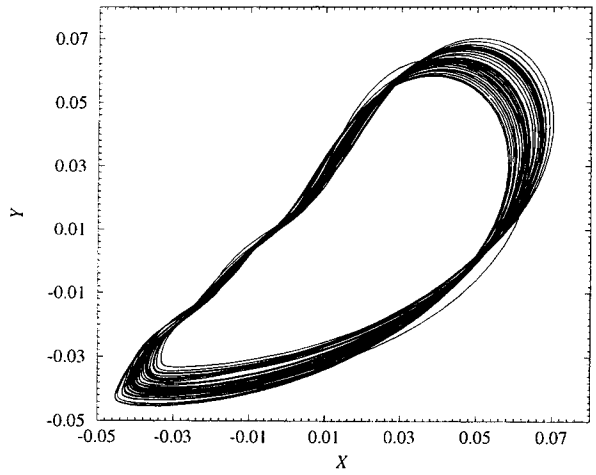

Figure 7. XY-plane projection of the phase portrait induced by the Rushton rotator ($f_p = 8.80$ Hz) by using a v_D-time series.

$$\begin{cases} X(t) = v_T(t) \\ Y(t) = v_T(t+\tau) \\ Z(t) = v_T(t+2\tau) \\ W(t) = v_T(t+3\tau) \end{cases} \tag{4}$$

where $\tau = 10/f_s \approx 9.76$ ms. An XY-plane projection of the phase portrait is displayed in Figure 7.

Poincaré section

A dynamical characterization of the phase portrait may be achieved by using a Poincaré section P defined by

$$P \equiv \{(Y, Z, W) \epsilon \mathbb{R}^3 \mid X = 0, \dot{X} < 0\} \tag{5}$$

From this Poincaré section which is 3-D since the phase space is 4-D, we build a first-return map by using the variable Y. This first-return map, displayed in Figure 8, presents a circular configuration which is a signature of a torus or near-

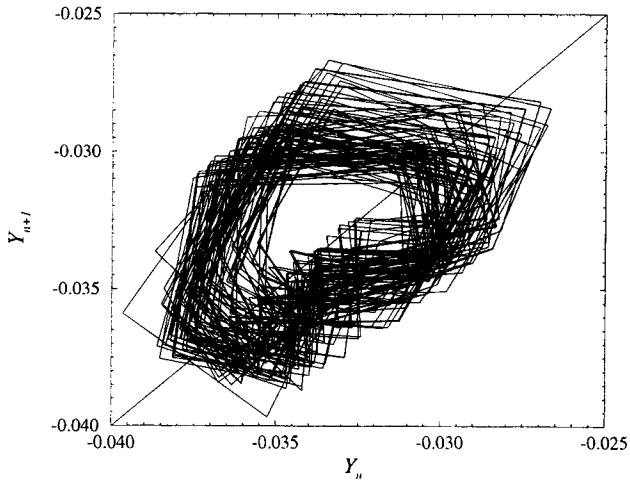

Figure 8. First-return map to the Poincaré section P.

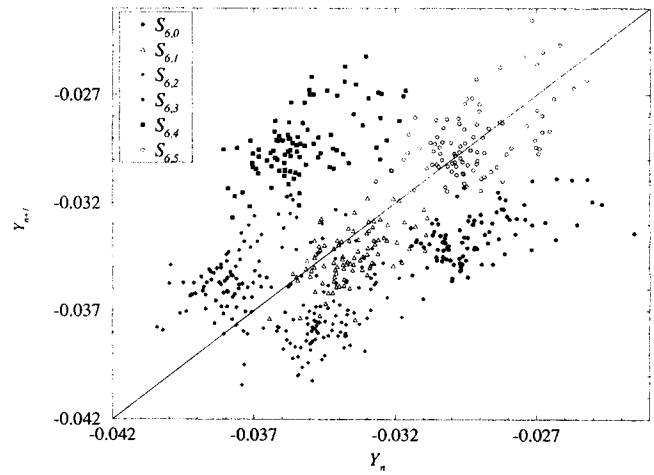

Figure 9. Six sets of points are exhibited evidencing the frequency $f_t = f_p/6$.

torus motion. In order to exhibit a characteristic frequency associated with this circular configuration map, we define sets of points from the first-return map as follows:

$$S_{p,k} = \left\{(Y_q, Y_{q+1}) \in \mathbb{R}^2 \mid q = np + k\right\}$$
$$\text{for } k \epsilon [0, p-1] \text{ and } n \in [1, N_p] \tag{6}$$

where N_p is the number of points in the Poincaré section. In Eq. 6, p is an integer variable allowing the description of p-periodicities in the map. The set of points $S_{1,0}$ is the first-return map itself. Increasing p from 1 up, it is discovered that well defined and separated sets of points are observed for $p = 6$ as exhibited in Figure 9.

Here, for instance, we have

$$S_{6,0} = \{(Y_0, Y_1), (Y_6, Y_7), (Y_{12}, Y_{13}, \ldots)\}$$
$$S_{6,1} = \{(Y_1, Y_2), (Y_7, Y_8), (Y_{13}, Y_{14}, \ldots)\}$$

and so on. Because the characteristic time between two successive returns to the Poincaré section is f_p^{-1}, Figure 9 exhibits the existence of another characteristic frequency $f_p/6$ which is identical to the rotator frequency f_t.

We now analyze the dynamical behavior of each set of points $S_{6,k}$. This is achieved by using a sixth-return map, removing the periodicity of order 6 involved in Figure 9. For instance, Figure 10 displays the result which is obtained on the set $S_{6,5}$. This Figure 10 does not exhibit any regular structure and, consequently, the variations in sets $S_{6,k}$ are not governed by a low-dimensional deterministic dynamics.

Comparison with the unfiltered dynamics

The analysis of the filtered dynamics allowed us to recover a deterministic contribution in the velocity field. Now that this contribution is isolated and characterized, we may wonder whether it can also be at least partially recovered from the unfiltered signal, too. This section is devoted to this issue.

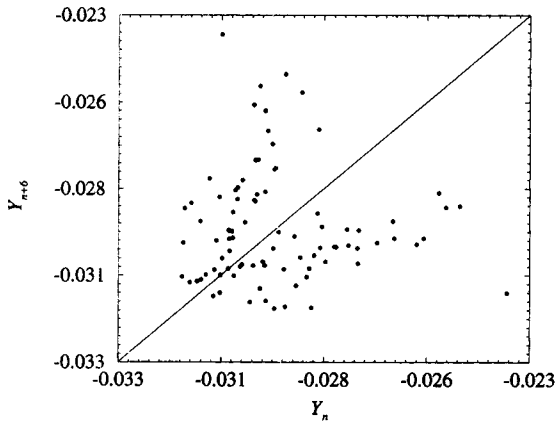

Figure 10. Sixth-return map to the Poincaré section *P* computed on the set $S_{6,5}$.

For the unfiltered signal, the *XY*-projection exhibited in Figure 7 becomes the one exhibited in Figure 11. As a whole, the overall structure of the dynamics is still well visible but due to the action of small turbulent structures, the trajectory has become jittery.

The power spectrum, obtained by averaging over four spectra each computed with 2^{14} points, is displayed in Figure 12, to be compared with Figure 4. We may still easily identify the fundamental frequencies f_p, f_t, f' associated with the previously characterized deterministic contribution, as well as the combinations $(f_p - f')$, $(f_p + f')$, $(f_p - f_t)$, $(f_p + f_t)$, but the background noise level has increased. Also, when the dynamics is analyzed in the Poincaré section *P* discussed earlier, the circular configuration of the first-return map, exhibited in Figure 8, is dispersed by the stochastic component of the dynamics and does not appear anymore. Figure 13 then shows an erratic set of points where the underlying deterministic structure is no longer apparent.

This fact is related to the behavior of correlation dimensions previously evaluated from the original time series (Kemoun, 1995). Indeed, with the unfiltered signal v_T, no

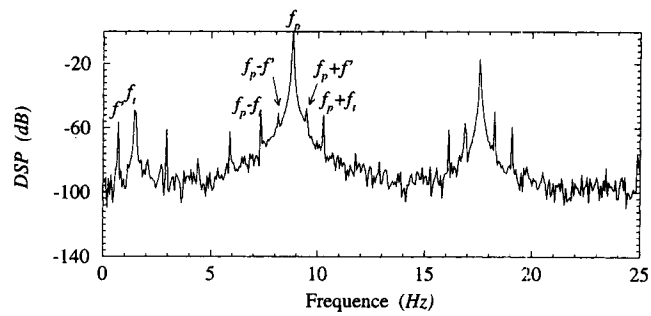

Figure 12. Power spectrum averaged over four spectra computed with 2^{14} points from the unfiltered $v_T(t)$-time series.

saturation of the computed correlation dimensions vs. the embedding dimension is observed in contrast to the case of the deterministic component v_D previously discussed. Moreover, the random part of the signal is not due to instrumental noise but is associated with the small scales of the turbulence. This is suggested by the relevance of the Kolmogorov length scales determined from the residue of the Hilbert transfer (Kemoun, 1995). Even if the standard deviation associated to this residue only represents 13% of the one of v_T, the small-scale turbulence is able to hide the deterministic behavior.

Global Vector Field Reconstruction

Theoretical background

It has been demonstrated that a set of ordinary differential equations can be automatically reconstructed from a deterministic scalar time series (Gouesbet and Maquet, 1992; Brown et al. 1994; Gouesbet and Letellier, 1994; Tufillaro et al., 1995; Letellier et al. 1995, and references therein), a process which is called global vector field reconstruction leading to a model. As for a phase space reconstruction, the model may be equivalently reconstructed by using delay coordinates (Brown et al., 1994; Serre et al., 1996), derivative coordinates (Gouesbet and Letellier, 1994) or also principal components

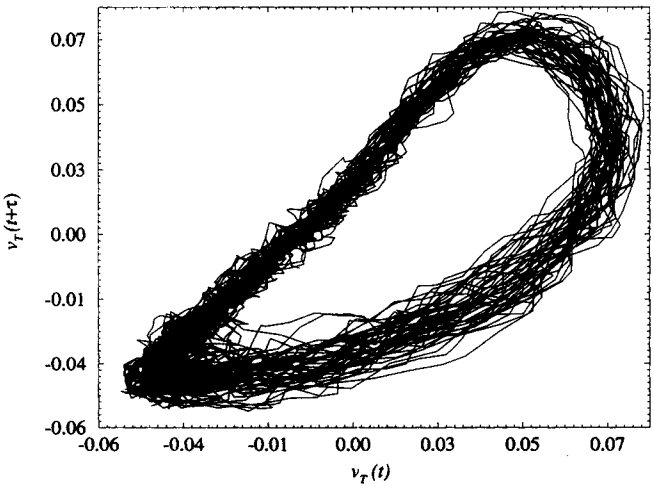

Figure 11. Plane projection of the unfiltered dynamics induced by the velocity field in the mixing tank (compare with Figure 7).

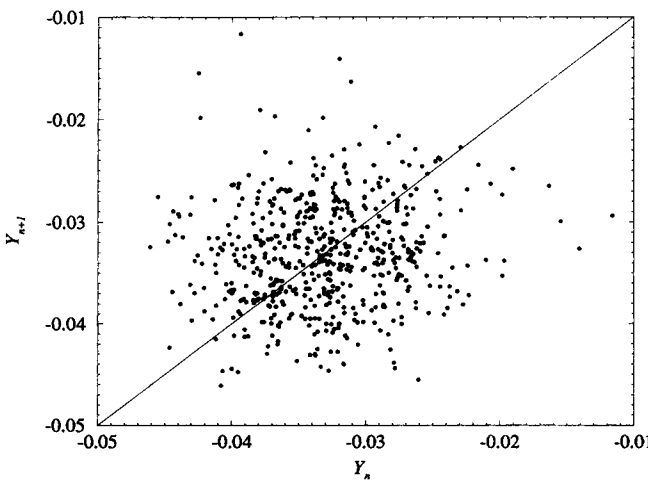

Figure 13. First-return map to the Poincaré section *P* computed from the unfiltered data.

since it has been shown that all these choices of coordinates are equivalent (Gibson et al., 1992). Here, we use derivative coordinates. Consequently, the model is based on the measured time series $x(t)$ and on its successive derivatives $\dot{x}(t)$, $\ddot{x}(t)$, . . . and may then be written as

$$\begin{cases} \dot{X}_1 = X_2 \\ \dot{X}_2 = X_3 \\ \vdots \\ \dot{X}_{d_E} = F(X_1, X_2, \ldots, X_{d_E}) \end{cases} \tag{7}$$

where d_E is the embedding dimension and F, the so-called standard function, depends on d_E variables which are successive derivatives

$$\begin{cases} X_1 = x(t) \\ X_2 = \dot{x}(t) \\ X_3 = \ddot{x}(t) \\ \vdots \end{cases} \tag{8}$$

The standard function F is approximated by using a multivariable polynomial basis on nets (Gouesbet and Letellier, 1994) which may be built by means of a Gram-Schmidt orthogonalization procedure (Letellier et al., 1997). The algorithm requires the definition of reconstruction parameters which are (i) the dimension d_E of the embedding space, (ii) N_q, the number of vectors $(X_{1,i}, X_{2,i}, \ldots X_{d_E,i}, \dot{X}_{d_E,i})$ $(i \in [1, N_q])$ on the net, with i a time index, (iii) δt, the time step between two successive such vectors, (iv) N_s, the number of vectors sampled per pseudo-period, (v) N_p, the number of retained multivariate polynomials and (vi) p, the window size on which the derivatives are estimated by using a sixth degree interpolation polynomial. These interpolation polynomials are built, centered at each point, by using the six nearest neighbors. Derivatives are then obtained by analytically deriving these polynomials. The window size p is taken to be equal to 7 times δt. The estimated standard function, denoted as $\tilde{F}$, then reads as

$$\tilde{F}(X_1, \ldots, X_{d_E}) = \sum_{p=1}^{N_p} K_p \Phi^p \tag{9}$$

where Φ^p is a multivariate monomial reading as

$$\Phi^p = X_1^{n_1} X_2^{n_2} \ldots X_{d_E}^{n_{d_E}} \tag{10}$$

in which the integers p are related to n_{d_E}-triplets $(n_1, n_2, \ldots, n_{d_E})$ by a bijective relationship discussed in Gouesbet and Letellier (1994).

Once the model is built, we obtain a reconstructed phase portrait by integrating the reconstructed vector field. One of the issues to be considered is then the validity of the model. When the embedding dimension d_E is equal to 3, our favorite method for validation is the topological characterization based on knot theory (Mindlin et al., 1991; Letellier et al., 1995). Unfortunately, in the present case where $d_E = 4$, no topological characterization is available at the present time. We shall then have to rely on a less sophisticated, albeit convincing enough, validation approach. We here insist on the fact that $d_E = 3$ is a limit of the validation by topological characterization, not a limit of global vector field reconstruction techniques.

Model from tangential component

Similarly as in the subsection on the phase portrait where we reconstructed a phase space by using time-delay coordinates, we now reconstruct a phase space by using derivative coordinates of the v_D-time series. In this section, the reconstructed phase space obtained in such a way is called the original phase space. Since we are expecting $d_E = 4$, we use four derivative coordinates reading as

$$\begin{cases} X(t) = v_D(t) \\ Y(t) = \dfrac{d\, v_D(t)}{dt} \\ Z(t) = \dfrac{d^2\, v_D(t)}{dt^2} \\ W(t) = \dfrac{d^3\, v_D(t)}{dt^3} \end{cases} \tag{11}$$

The 4D-phase portrait is then visualized by displaying the six available plane projections (Figure 14).

We next achieve a global vector field reconstruction following the scheme described in the previous section. The recon-

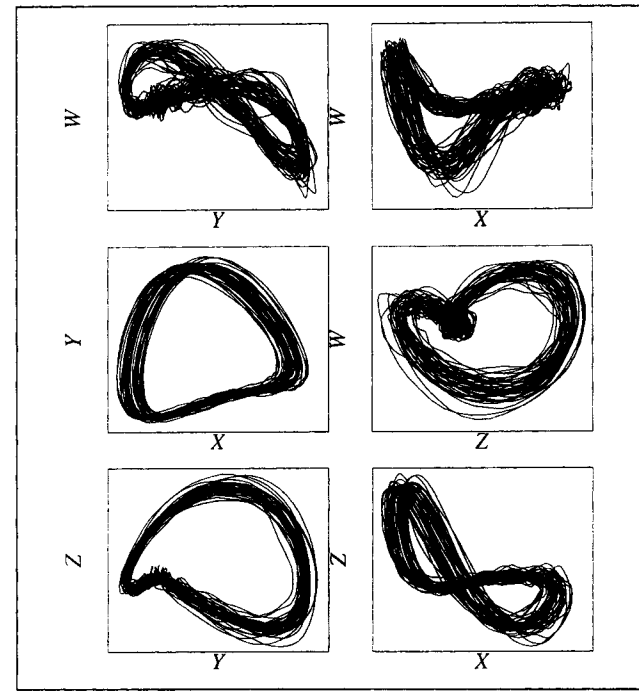

Figure 14. Six plane projections of the original phase space spanned by derivative coordinates of measured time series.

struction parameters are determined with the aid of an error function E_r to be (at least locally) minimized, reading as

$$E_r = \frac{\sum_{i=1}^{N_q} |\dot{W}_i - \tilde{F}(X_i, Y_i, Z_i, W_i)|}{\sum_{i=1}^{N_q} |\dot{W}_i|} \tag{12}$$

This error function is computed by using absolute values for the sake of computational efficiency. A good approximation $\tilde{F}$ of the function F is found with reconstruction parameters given by

$$\begin{cases} N_q = 1{,}410 \\ N_s = 10 \\ N_p = 65 \end{cases} \tag{13}$$

The time step δt is the inverse of the sampling rate f_s. The vector field reconstruction is applied to the deterministic part of the tangential component extracted by the Hilbert transform. The coefficient spectrum $\{K_p\}$ is reported in Table 2. It must be understood that the reconstructed object (as the original one) possesses what we call a high degree of internal nonlinear coherence which would be destroyed by a small perturbation of the reconstructed vector field. Only the dimension of the model is here generic. However, improvements in the robustness along lines suggested in Aguirre and Billings (1995) to avoid overparametrization could possibly be implemented in the future.

Beside, it must be emphasized that this example of global vector field reconstruction is a particularly difficult one for several reasons: (i) the original time series comes from an experimental complex dynamics which, although filtered, must still contain a small amount of noisy data; (ii) the phase space is of dimension 4, requiring the use of derivatives up to fourth order, amplifying the original residual noise. As a consequence, due to the resulting lack of stability, the model cannot be integrated beyond 2,000 time steps approximately correspondings to 20 pseudo-periods (integration is carried out by using an adaptative stepsize Runge-Kutta scheme). The trajectory hereafter diverges to the infinity.

The integrated trajectory is displayed in Figure 15 using the same plane projections as for the original system. Figures 14 and 15 compare very favorably. Therefore, although lacking robustness, the reconstructed model correctly captures essential structural features of the dynamics. The visual comparison between original and reconstructed plane projections provides a validation of the model.

Another possible validation (in principle) would be to analyze the reconstructed trajectory by using the same tools for the original trajectory that we used in the section discussing dynamical analysis. However, the reconstructed time series is not robust enough to allow such a validation in a complete way. Nevetheless, it is to be noted that, during the first ten pseudo-periods (that is, approximatively half of the reconstructed signal), the first-return map is quite similar to the original one and allows the exhibit the six sets $S_{6,k}$, $(k = 0, \ldots 5)$ shown in Figure 9. Beyond this time, the sets $S_{6,k}$ are no longer visited in the same order as in the original dynamics, indicating that the reconstructed dynamics starts to significantly depart from the original one.

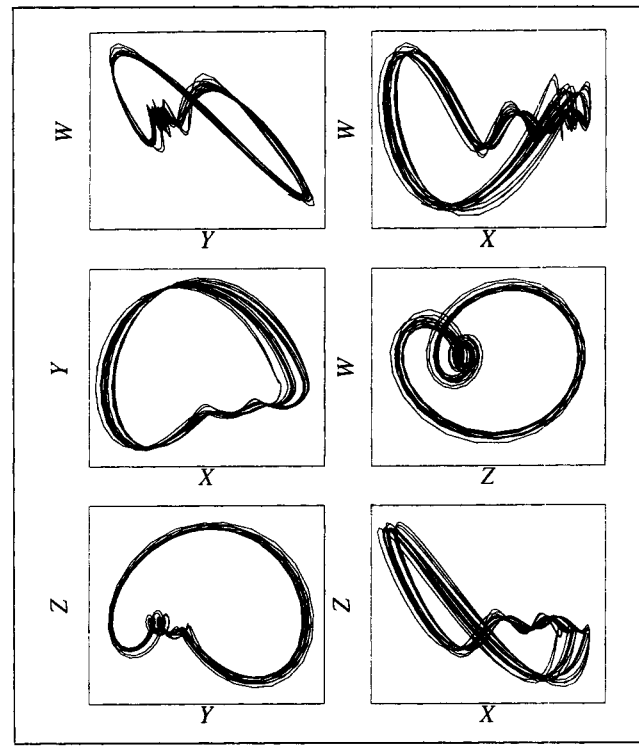

Figure 15. Six plane projections of the phase portrait obtained by integrating the reconstructed model.

Indeed, improvements of global vector field reconstruction techniques allowing to obtain more robust reconstructions to facilitate the investigation of more complex dynamics is a current active field of research. However, for the present state of the art, the success of our reconstruction (even if it is partial) provides further support to our conclusion that we have indeed isolated a deterministic component in the experimental data. Furthermore, global vector field reconstructions have been attempted for an embedding dimension $d_E = 3$, but without any success. This result provides a confirmation of our conclusion that the dynamics associated with the small frequencies (large eddies) takes place in a phase space having $d_E = 4$. As long as the model remains 4-D when the control volume is moved along the radius, only four variables are required to describe the dynamics associated with the deterministic component of the velocity field. There exists then the possibility that the large eddy structure could be modeled by a global vector field model to be incorporated in a code for turbulence predictions, in which the small scales of turbulence would be described by a stochastic approach.

Conclusion

It is known that developed turbulence may be considered as resulting from the coupled contributions of large eddy structures (deterministic component) and of small eddy structures (stochastic component). This point of view is, for in-

stance, used in turbulence modeling using LES (large eddy simulation). In the case of a complex velocity field produced by a standard mixing reactor, the deterministic component associated with large eddy structures has been extracted in two steps. First, an identification method starting from the extraction of the carrier frequency modulation is applied to the tangential component of the velocity field time series v_T recorded in a measured volume located 5 mm from the blades by a LDA measuring technique. Second, a set of four ordinary differential equations which models the dynamical behavior of the deterministic component of the velocity field given by the Hilbert transform is obtained. Such a model is extracted with a global vector field reconstruction technique. As required by this method, the four variables of the model are observable for the measured time series v_T and its first three time derivatives. It is to be noted that the dynamical behavior depends on the location of the control volume. If such a model, however, remains valid on a large range of radii, then the large eddy structures of the weakly turbulent flow could possibly be simulated by a low-dimensional deterministic model. This model could be used in association with a code of prediction incorporating a stochastic approach to small-scale behaviors.

The approach developed in this article is actually quite general and may be used for modeling many deterministic behaviors of experimental low-dimensional systems. In particular, global vector field reconstruction techniques have been successfully applied to a copper electrodissolution in phosphoric acid (Letellier et al., 1995), a Belousov-Zhabotinskii reaction (Le Sceller, 1997), a string experiment (Brown et al., 1994), electronic circuits (Aguirre and Billings, 1995), among others.

Literature Cited

Abarbanel, H. D. I., R. Brown, J. J. Sidorowich, and L. Sh. Tsimring, "The Analysis of Observed Chaotic Data in Physical Systems," *Rev. of Modern Phys.*, **65**(4), 1331 (1993).

Aguirre, L. A., and S. A. Billings, "Improved Structure Selection for Nonlinear Models Based on Term Clustering," *Int. Control*, **62**(3), 569 (1995).

Aguirre, L. A., and S. A. Billings, "Dynamical Effects of Overparametrization in Nonlinear Models," *Physica D*, **80**, 26 (1995).

Hao Bai Lin. *Elementary Symbolic Dynamics and Chaos in Dissipative Systems*, World Scientific Publishing, Singapore (1989).

Brown, R., N. F. Rul'kov, and E. R. Tracy, "Modeling and Synchronizing Chaotic Systems from Time-Series Data," *Phys. Rev. E*, **49**(5), 3784 (1994).

Buzug, T., and G. Pfister, "Optimal Delay Time and Embedding Dimension for Delay-Time Coordinates by Analysis of the Global Static and Local Dynamical Behavior of Strange Attractors," *Phys. Rev. A*, **45**(10), 7073 (1992).

Collet, P., and J. P. Eckmann, "Iterated Maps on the Interval as Dynamical Systems," Prog. in Physics, A. Jaffe et D. Ruelle, ed., Birkhäuser, Boston (1980).

Fraser, A. M., and H. L. Swinney, "Independent Coordinates for Strange Attractors from Mutual Information, *Physical Rev. A*, **33**(2), 1134 (1986).

Gibson, J. F., J. D. Farmer, M. Casdagli, and S. Eubank, "An Analytical Approach to Practical State Space Reconstruction," *Physica D*, **57**, 1 (1992).

Gouesbet, G., and J. Maquet, "Construction of Phenomenological Models from Numerical Scalar Time Series," *Physica D*, **58**, 202 (1992).

Gouesbet, G., and C. Letellier, "Global Vector Field Reconstruction by Using a Multivariate Polynomial L_2-Approximation on Nets," *Phys. Rev. E*, **49**(6), 4955 (1994).

Grassberger, P., and I. Proccacia, "Measuring the Strangeness of Strange Attractors," *Physica D*, **9**, 189 (1983).

Hall, T., "The Creation of Horseshoes," *Nonlinearity*, **7**(3), 861 (1994).

Kemoun, A., "Caractérisation Expérimentale de la Structure de l'Écoulement dans une Cuve Agitée: Mélange," PhD Thesis, INPL, Nancy (1995).

Le Sceller, L., "Reconstruction Globale de Champ de Vecteurs et Applications," PhD Thesis, LESP, Rouen Univ. (Feb. 28, 1997).

Letellier, C., L. Le Sceller, P. Dutertre, G. Gouesbet, Z. Fei, and J. L. Hudson, "Topological Characterization and Global Vector Field Reconstruction from Experimental Electrochemical System," *J. Phys. Chemistry*, **99**, 7016 (1995).

Letellier, C., and G. Gouesbet, "Topological Characterization of Reconstructed Attractors Modding Out Symmetries," *J. Physique II*, **6**, 1615 (1996).

Letellier, C., E. Ringuet, B. Maheu, J. Maquet, and G. Gouesbet, "Global Vector Field Reconstruction of Chaotic Attractors from One Unstable Periodic Orbit," *Entropie*, **202/203**, 147 (1997).

Melville, W. K., "Wave Modulation and Breakdown," *J. Fluid Mech.*, 128, 489 (1983).

Mindlin, G. B., H. G. Solari, M. A. Natiello, R. Gilmore, and X. J. Hou, "Topological Analysis of Chaotic Time Series Data from the Belousov-Zhabotinski Reaction," *J. Nonlin. Sci.*, **1**, 147 (1991).

Oppenheim, A. V., and R. W. Schafer, *Digital Signal Processing*, Prentice-Hall, Englewood Cliffs, NJ (1975).

Packard, N. H., J. P. Crutchfield, J. D. Farmer, and R. S. Shaw, "Geometry from a Time Series," *Phys. Rev. Letters*, **45**(9), 712 (1980).

Poincaré, H., *Oeuvres Complètes*, Gauthier-Villars, Paris (1952).

Serre, T., Z. Kolláth and J. R. Buchler, "Search For Low-Dimensional Nonlinear Behavior In Irregular Variable Stars—The Analysis of Irregular W Vir Model Pulsations," *Astronomy Astrophysics*, 311, 845 (1996).

Takens, F., "Detecting Strange Attractors in Turbulence," *Dynamical Systems and Turbulence, Warwick 1980*, Lecture Notes in Mathematics, Vol. 898, D. A. Rand and L. S. Young, eds., Springer-Verlag, Berlin (1980).

Tufillaro, N. B., P. Wyckoff, R. Brown, T. Schreiber, and T. Molteno, "Topological Time Series Analysis of a String Experiment and its Synchronized Model," *Phys. Rev. E*, **51**(1), 164 (1995).

Manuscript received Dec. 31, 1996, and revision received June 2, 1997.